Pergamon

*Solid-State Electronics* Vol. 42, No. 10, pp. 1881–1891, 1998

Printed in Great Britain

PII: S0038-1101(98)00166-X

0038-1101/98/$ - see front matter

# AN EFFICIENT TRANSIENT MODELING FOR 3-D MULTILEVEL INTERCONNECTIONS IN A STRATIFIED DIELECTRIC MEDIUM

CHING-YUAN WU and HSIN-MING HOU

Advanced Semiconductor Device Research Laboratory, Institute of Electronics, National Chiao-Tung University, 1001 Ta-Hsueh Road, Hsin-Chu, 300, Taiwan, R.O.C.

*(Received 12 February 1998)*

**Abstract**—An efficient method is presented to model the transient characteristics of distributed resistor–capacitor of ULSI multilevel interconnections on complex topography, in which the reformulation of the boundary-element method (BEM) associated with the Padè-via-Lanczos (PVL) algorithm can avoid the redundant works on both volume mesh and transient analysis associated with the finite-difference method. An adaptive multilayer closed-form spatial Green's function for BEM is developed to examine the voltage and current responses of the multilevel conductor system by using the boundary-element method of integral formulation, in which arbitrary triangular elements on the surface of conductors are used to efficiently calculate the free-charge distributions of complex structure based on actual topography/processes. Applying the Galerkin principle over boundary elements, all of the surface integrals of charge distribution have been discretized and evaluated analytically for constant element. To improve the timing-analysis efficiency of the finite-difference method, the dominant poles are obtained by introducing the Padè-via-Lanczos (PVL) algorithm for model-order reduction. Hence, it is easy to calculate the transient characteristics of both parallel conductors and complicated configurations such as crossing lines, corners, contacts, multilayers and their combinations. Therefore, a simple and more general method is proposed for solving the combinations of complex structures based on actual topography/processes and arbitrary geometric configurations of multilevel interconnection lines in order to link with the present CAD tools. © 1998 Published by Elsevier Science Ltd. All rights reserved

## 1. INTRODUCTION

As the feature sizes of integrated devices are scaled down, the response time of ULSI chip is increasingly determined by the interconnection[1,2]. The IC interconnection delay modeled with high accuracy in ULSI circuits becomes more and more important and necessary. The geometry of the interconnection is an important factor in the transmission behavior and is also essential for the layout-to-circuit extractors to obtain accuracy and efficiency. In a software tool called Space[3], the interconnections are subdivided into small elements and each element is replaced by a lumped RC-section. However, the number of elements must be sufficiently large to guarantee that the distributed properties of the interconnection are accurately reflected by the resulting network, and an enormous amount of memory employed due to a large number of the extracted section will not result in efficient timing analysis. In the past, it was suggested that simulations with sufficient accuracy based on asymptotic waveform evaluation (AWE)[4] could be performed by computing the transient characteristics of the electric fields both inside and outside the interconnects by the finite-difference discretization of Laplace equation[5]. However, this method is time-consuming and the ill-conditioned problem of matching the moments for the AWE method will explicitly happen. Recently, the boundary-element approach based on Green's theorem, which has been widely applied to important issues of interconnections but can avoid the volume mesh associated with the finite-difference methods, has been investigated by many research groups[6–10]. Furthermore, to analyze the transient characteristics of the interconnections placed in complex topography becomes an even more complicated and difficult task.

To deal with these problems, an efficient and accurate modeling of transient characteristics of different dielectric layers for such a densely packed multiconductor system has been developed. Based on the conservation of charge[10], the boundary-element integral can be reformulated by time-dependent integral formulation. Nevertheless, arbitrary triangular elements on the surface of conductors for charge distribution are adopted to calculate the free-charge distribution for arbitrary configurations of multilevel conductor system in a inhomogeneous medium, and the actual topography of multilevel conductor system becomes more realistic in modeling its transient characteristics. For this purpose, our work uses an adaptive multilayer closed-form

spatial Green's function[13] for BEM to examine the voltage and current responses of multilevel conductor system. By introducing the closed-form spatial Green's function, we can efficiently deal with the number of layer more than three, as compared with the method using the full- form Green's function in Ref.[9]. Applying the Galerkin principle over boundary elements, all of the surface integrals of charge distribution have been discretized and evaluated analytically for constant element. After the Laplace transformation of the large linear equations, all the poles and residues can be obtained by diagonalization of matrix. To improve timing analysis efficiency, the Padè-via-Lanczos (PVL) algorithm[11] is introduced to generate arbitrary numbers of poles and residues with little numerical degradation. Besides, this method can avoid the ill-conditioned problem of matching the moments induced explicitly by the AWE method. The formulations of poles and residues are derived, which can be calculated fast enough to easily include in a circuit simulator. Hence, it is easy to calculate transient characteristics of both parallel conductors and complicated configurations such as crossing lines, corners, contacts, multilayers and their combinations. At the same time, we find that the transient characteristics of the interconnection strongly depend on its capacitance obtained by Ref.[7] for steady state. Major improvements are the reformulation of BEM and PVL with multilayer closed-form spatial Green's function to model the transient characteristics, which are proven to be applicable to even more complex configuration.

## 2. MATHEMATICAL FORMULATION

### 2.1. *Green's formulation*

It is adequate to assume that the relaxation time of the volume charge is short enough to be negligible so that we only consider the transient response of surface charge. The BEM for calculating multiconductor transient characteristics is based on Green's function approach to the electrostatic problem. Consider a geometry with a number of conductors embedded in a perfectly stratified dielectric medium, the multilayer Green's function $G(x, x_s)$ can be obtained. For a view point $x$ and a source point $x_s$, let us define the potential $V(x)$, the dielectric constant $\varepsilon(x)$, $\nabla_{x_s} = \partial/\partial n_{x_s}$ the derivative along the outward normal $n_{x_s}$ to the boundary surface $S(x_s)$. From the Laplace equation $\nabla^2 V \equiv 0$ and its Green's function defined as $\nabla^2 G \equiv -\delta/\varepsilon(x_s)$, one can obtain the boundary integral equation:

$$c(x)V(x)+\int_S V(x_s)\varepsilon(x_s)\nabla_{x_s}G(x,x_s)\cdot \mathrm{d}\boldsymbol{S} = \int_S G(x,x_s)\varepsilon(x_s)\nabla_{x_s}V(x_s)\cdot \boldsymbol{n}\mathrm{d}S, \quad (1)$$

where $c(x)$ is equal to 1/2 due to singularity integral for the view point $x$ on boundary, otherwise $c(x) = 1$ for the view point $x$ on bulk.

Decompose the second integral in Equation (1) into contact $S_c$ and floating (non-contact) $S_f$ surface integrals, as represented by $\int_S = \int_{S_c} + \int_{S_f}$. For the view point $x$ on the non-contact (floating) and contact surface of conductors, the conservation of charges[10] can be written by the following equations, respectively:

$$-\frac{\partial \rho_f}{\partial t} = J_{\mathrm{normal}}(x_f) - \sigma\nabla_{x_f}V(x_f) \quad (2)$$

and

$$-\frac{\partial \rho_c}{\partial t} = -\sigma\nabla_{x_c}V(x_c) - J_{\mathrm{external}}(x_c), \quad (3)$$

where $\sigma$ is the conductivity of conductor; $J_{\mathrm{normal}}(x)$ is the current density along the inward directed normal to the conductor surface; $J_{\mathrm{external}}(x)$ is the current density supplied to the conductor through the contact; and $\nabla_x V(x)$ is the spatial derivative of $V$ along the inward directed normal to the conductor surface. For the wavelength of electromagnetic wave longer than the length of conductor, the magnetic fields can be neglected and Equation (1) is derived by the following expression:

$$\tau(x)\frac{\partial V(x)}{\partial t} = c(x)V(x) + \int_S V(x_s)\varepsilon(x_s)\nabla_{x_s}G(x,x_s)\cdot \mathrm{d}\boldsymbol{S} + \int_{S_c} G(x,x_c)\tau(x_c)J_{\mathrm{external}}(x_c)\mathrm{d}S_c, \quad (4)$$

where $\tau = \varepsilon/\sigma$ is the dielectric relaxation time.

Let the external charge at the contact region be defined as

$$\rho_{\mathrm{external}}(x_c) = \tau(x_c)J_{\mathrm{external}}(x_c). \quad (5)$$

After discretization of Equation (4), the surface of conductors is divided into $N$ elements and the meshing number of the contact part of the conductor surface is $M$. Generally, the charge density $\rho_{\mathrm{external}}(x_j)$ on conductors can be described by the shape function $f_k(x_j)$ and the charge of the $k$th element $\rho_k(x_k)$, where the index "$k$" denotes the $k$th element of the contact surface of conductors. To make the calculation more efficient under tolerable error, it is taken to be a piecewise constant distribution over a set of the triangular elements, as described by

$$\rho_{\mathrm{external}}(x_j) = \sum_{k=1}^{M}\rho_k(x_k)f_k(x_j), \quad (6)$$

where $f_j(x_j)$ is the constant-element shape function assigned to the boundary element $S_j$ such that $\int_{S_j} f_j(x_j)\mathrm{d}S_j = 1$. The Galerkin method applied to the discretized boundary integral equation gives

$$\tau(x_i)\frac{\partial V(x_i)}{\partial t} = c(x_i)V(x_i) + \sum_{j=1}^{N}\int_{S_j} V(x_j)\varepsilon(x_j)\nabla_{x_j}G(x_i,x_j)\cdot \mathrm{d}\boldsymbol{S}_j + \sum_{j=1}^{M}\rho_j(x_j)\int_{S_j} G(x_i,x_j)f_j(x_j)\mathrm{d}S_j. \quad (7)$$

We choose the view point $x$ on boundary, so $c(x_i)$ is equal to 1/2 due to singularity integral. The above equation can be rewritten as

$$\tau(x_i)\frac{\partial V(x_i)}{\partial t} = \frac{1}{2}V(x_i) + \sum_{j=1}^{N}\int V(x_j)G_{ij}^{(n)} + \sum_{j=1}^{M}\rho_j(x_j)G_{ij}, \quad (8)$$

where the matrix element $G_{ij}=\int_{S_j} G(x_i,\ x_j)f_j(x_j)dS_j$ and the matrix element $G_{ij}^{(n)}=\int_{S_j}\varepsilon(x_j)\nabla_{x_j}G(x_i,\ x_j)f_j(x_j)\cdot\mathrm{d}\boldsymbol{S}_j$.

To obtain a concise form in matrix notation for the discretized boundary integral formulation, the above equation can be reformulated as

$$\tau\left[\frac{\partial V}{\partial t}\right] = [H_{ij}][V] + [G_{ij}][\rho], \quad (9)$$

where $[H_{ij}]=\frac{1}{2}[I] + [G_{ij}^{(n)}]$. Explicitly, $[V] = [V_1,\ V_2,\ \ldots,\ V_N]^T$ and $[\rho] = [\rho_1,\ \rho_2,\ \ldots,\ \rho_M]^T$ are the potentials and charges of element, respectively; $[I]$ is the identity matrix. After the Laplace transformation of the above equation, one can obtain the following expression:

$$\tau s\begin{bmatrix} V_c \\ V_f \end{bmatrix} = \begin{bmatrix} H_{cc} & H_{cf} \\ H_{fc} & H_{ff} \end{bmatrix}\begin{bmatrix} V_c \\ V_f \end{bmatrix} + \begin{bmatrix} G_{cc} \\ G_{fc} \end{bmatrix}[\rho_c], \quad (10)$$

where the index "$c$" denotes the contact region and "$f$" denotes the floating region. Define the Laplace transformation of the input excitation vector $[V_c]$ as $[b]u(s)$, we can obtain the contact charges of conductors as

$$[\rho_c] = \tau s[G_{cc}]^{-1}[b]u(s) - [G_{cc}]^{-1}[H_{cc}][b]u(s) - [G_{cc}]^{-1}[H_{cf}][V_f] \quad (11)$$

and the potential of the floating region on conductor as

$$[V_f] = \frac{[b_2]u(s)}{\tau} + (\tau s[I] - [A])^{-1}[v]u(s), \quad (12)$$

where $[A] = [H_{ff}] - [B_{fc}][H_{cf}]$, $[b_1] = ([H_{fc}] - [B_{fc}][H_{cc}])[b]$, $[b_2] = \tau[B_{fc}][b]$, $[B_{fc}] = [G_{fc}][G_{cc}]^{-1}$ and $[v] = [b_1] + [A][B_{fc}][b]$. To obtain transient behavior, the transfer function for voltage is defined as

$$H(s) = \frac{[l]^T[V_f(s)]}{u(s)}, \quad (13)$$

where $[l]^T\in R^{N-M}$ is the vector which picks out the voltages from a specific observation point. By combining the above two equations, we immediately obtain

$$H(s) = k + [l]^T(\tau s[I] - [A])^{-1}[v], \quad (14)$$

where $k = [l]^T[b_2]/\tau$. Besides, the transfer function for current can be defined as

$$H(s) = \frac{[L]^T[J_{\text{external}}(x_c,s)]}{u(s)}, \quad (15)$$

where $[L]^T\in R^M$ is the vector which picks out the currents from a specific observation point. By combining Equations (5) and (11) and the above equation, we also get

$$H(s) = k_0 + sk_1 - \frac{1}{\tau}[L]^T[G_{cc}]^{-1}[H_{cf}](\tau s[I] - [A])^{-1}[v], \quad (16)$$

where $k_0 = -(1/\tau)[L]^T[G_{cc}]^{-1}[H_{cc}][b] - (1/\tau^2)[L]^T[G_{cc}]^{-1}[H_{cf}][b_2]$ and $k_1 = [L]^T[G_{cc}]^{-1}[b]$.

### 2.2. *Padè-via-Lanczos (PVL) algorithm*

Using the Padè-via-Lanczos (PVL) algorithm[11], the reduced-order transfer function for Equation (14) can then be constructed as

$$H_q(s) = k + [l]^T[v][e_1]^T(\tau s[I] - [T_q(s)])^{-1}[e_1], \quad (17)$$

which is just the $q$th Padè approximation of $H$, whereas $[e_1] = [100\ldots0]^T\in R^q$, $[T_q(s)]$ is the tridiagonal matrices and $q\times q$ upper Hessenberg matrix. The transfer function of the reduced $q$th-order system can be obtained directly by using the eigen-decomposition $[S_q][diag(\lambda_1,\ \lambda_2,\ \ldots,\ \lambda_q)][S_q]^{-1}$. After manipulation, we can obtain

$$H_q(s) = k + \sum_{j=1}^{q}\frac{R_j}{s - P_j}, \quad (18)$$

where $[\mu]^T=[e_1]^T[S_q]$ and $[v] = [S_q]^{-1}[e_1]$. The $j$th pole and the $j$th residue of $H_q(s)$ are $P_j=\lambda_j/\tau$ and $R_j=[l]^T[v]\mu_j v_j/\tau$, respectively.

Similarly, the reduced-order transfer function for Equation (16) can be also derived by the PVL algorithm. Furthermore, the pole/residue representation of the Padè approximation of $H_q$ can be obtained by running the Lanczos algorithm and by computing an eigen decomposition of the Lanczos matrix $T_q$. As the number of computed poles $q$ is increased, one can see more and more accurate approximation of the poles. At the same time, the $H_q$ approximation form is more and more approaching the exact frequency response $H$. It is noted that both the pole and residue formulations are concise and are easy to link with the present CAD tools.

### 2.3. *Closed-form Green's function*

The derivations given in the above sections can be used when there is the multilayer region.

Generally, the problem of an appropriate 3-D Green's function in the multilayer region can be obtained by the proper closed-form integrations. The closed-form expression of the electrostatic Green's functions for a point charge derived in this section is based on the approach used in[13]. We consider that the interconnections are placed in a $N$ dielectric stratified medium over an electric ground plane as depicted in Fig. 1. This assumption is valid when the substrate is heavily doped and the IC is reasonably planar. So, the Si-substrate is the infinite ground plane and the multidielectric layers, $SiO_2$ and $Si_3N_4$ layers, are used as protective material. The $N$th layer is a half-space and all dielectric layers and ground plane are assumed to be planar and infinite in the $xy$-plane. The electrostatic Green's function in the spatial domain is described by the following closed-form formula:

$$G(p,q) = \frac{1}{4\pi\varepsilon_m}\sum_{i=1}^{4} f_i^{\pm}(p,q). \tag{19}$$

For $i = 1$ and $z \geq z'$, the expression of $f_i^{\pm}(p, q)$ is given by

$$f_1^{+}(p,q) = \frac{K_{m,n,1}^{+,\infty}}{\sqrt{(x-x')^2+(y-y')^2+(z+z'-2d_n)^2}} + \sum_{j=1}^{N_{m,n,1}^{+}} \frac{C_{m,n,1}^{+,j}}{\sqrt{(x-x')^2+(y-y')^2+(z+z'-2d_n+a_{m,n,1}^{+,j})^2}} \tag{20}$$

where the superscripts + and − are used to denote the cases for $z \geq z'$ and $z \leq z'$, respectively. The parameter $K_{m,n,j}^{+}$ is approximated by $\sum_{j=1}^{N_{m,n,1}^{+}} C_{m,n,1}^{+,j} e^{a_{m,n,1}^{+,j}\gamma}$. This scenario has been described in[13]. $N_{m,n,1}^{+}$ is the number of exponential functions used to approximate $K_{m,n,1}^{+}$. Here a maximum number of exponentials used in the approximation is eleven.

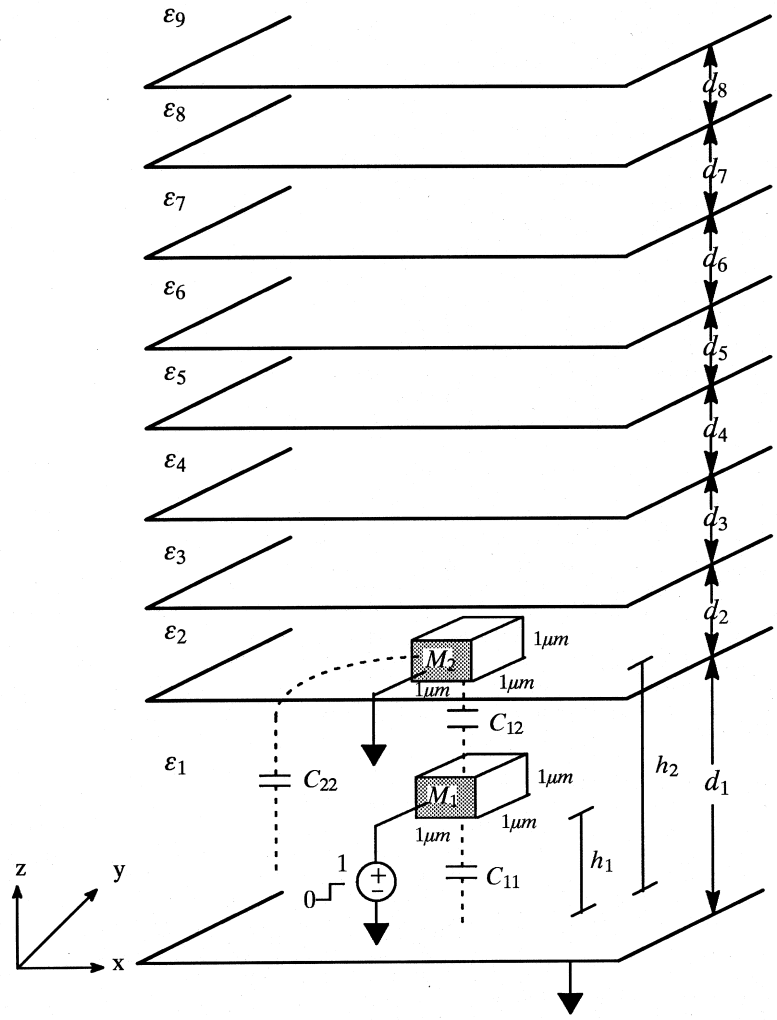


Fig. 1. The configuration of multilevel interconnections ($\rho_{\text{polysilicon}} = 0.01\ \Omega$ cm) in inhomogeneous medium over an infinite ground plane and its equivalent circuit.

$K^{+,\infty}_{m,n,1}$ denotes the asymptotic value of $K^{+}_{m,n,1}$. The first subscript $m$ denotes the layer where the source is located, whereas the second subscript $n$ will be used to denote the layer where the Green's function is evaluated. The parameter $\varepsilon_m$ denotes the dielectric constant of the $m$th layer and $d_n$ is the thickness of the $n$th layer. The source point $q(x', y', z')$ and the field point $p(x, y, z)$ are space variables, which are described in the rectangular coordinate shown in Fig. 1.

Finally, we note that considering the form of Equation (19), it can be seen that the exponentials used to approximate the Green's function in the spectral domain correspond to the weighted images in the space domain.

### 3. ELEMENT INTEGRATION

The constant flat boundary element system is used here. The boundary $\Gamma$ is approximated by a polyhedron of $N$ flat sides, i.e. $\Gamma = \Gamma_1 + \Gamma_2 + \ldots + \Gamma_N$. Here we choose the triangular element, so $N = 3$. The integral calculations of matrix element $G_{ij} = \int_{S_j} G(x_i, x_j) f_j(x_j) \mathrm{d}S_j$ and the matrix element $G^{(n)}_{ij} = \int_{S_j} \varepsilon(x_j) \nabla_{x_j} G(x_i, x_j) f_j(x_j) \cdot d\boldsymbol{S}_j$ in Equation (8) are the most critical part of a simulator, since it determines the computation time and the accuracy. For the constant boundary element, the integral terms of matrix elements, $G_{ij}$ and $G^{(n)}_{ij}$, are in analytical forms, which can be expressed as[12]

$$G^{(n)}_{ij} = \sum_{\Gamma_1}^{\Gamma_3} [\tan^{-1}(ZY) + sign(Z)\Delta\Theta] \tag{21}$$

$$G_{ij} = \frac{1}{2\varepsilon(x_j)A_j} \sum_{\Gamma_1}^{\Gamma_3} \left[ Dln \left| \frac{r_1 + r_2 + L}{r_1 + r_2 - L} \right| - |Z| \tan^{-1}(|Z|Y) + |Z|\Delta\Theta \right]$$

where $Y = (Dr_1 l_2 - r_2 l_1)/D_1^2 r_1 r_2 + z^2 l_1 l_2$ and

$$\Delta\Theta = \begin{cases} (a) & \text{corner angle} \\ (b) & 2\pi \\ (c) & 0 \end{cases} \tag{23}$$

in which the condition ($a$) in Equation (23) is the projection point on vertex; the condition ($b$) is the projection point on boundary or inside triangular

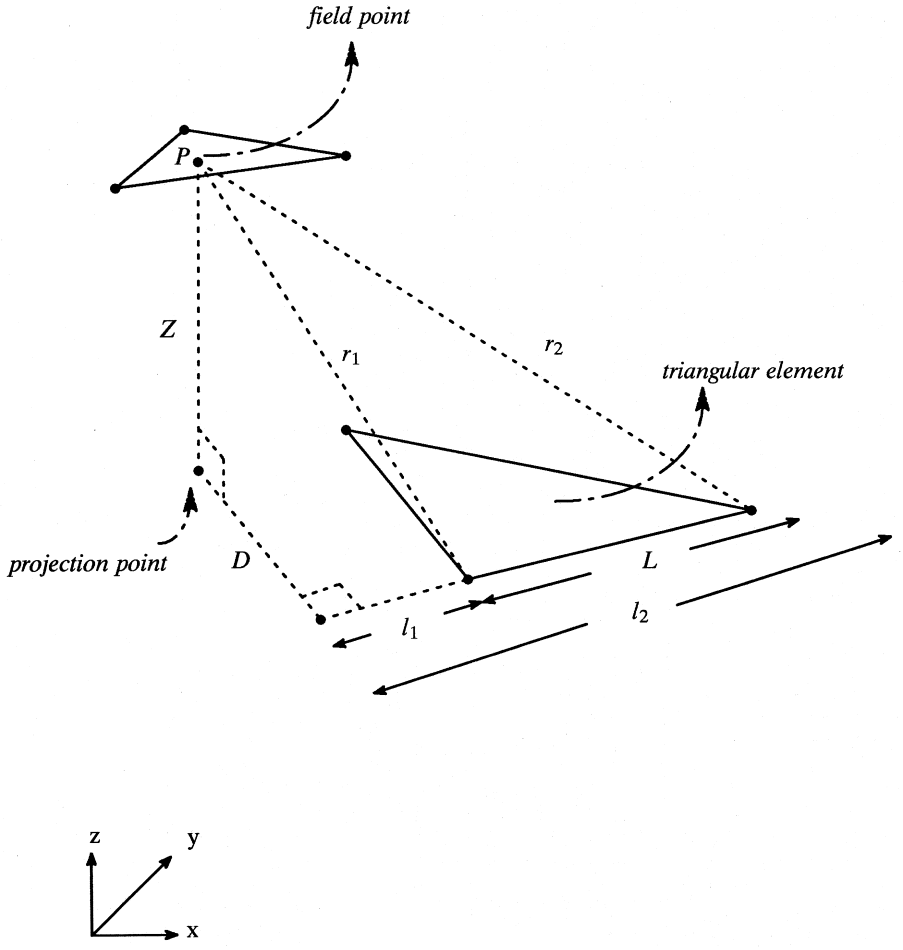


Fig. 2. The configuration of the field point and the triangular element based on three source points.

Table 1. The accuracy and the CPU time vs the total mesh number for Fig. 1. ($\varepsilon_1 = 12\varepsilon_0$, $\varepsilon_2 = 10\varepsilon_0$, $\varepsilon_3 = 8\varepsilon_0$, $\varepsilon_4 = 6\varepsilon_0$, $\varepsilon_5 = 5\varepsilon_0$, $\varepsilon_6 = 4\varepsilon_0$, $\varepsilon_7 = 3\varepsilon_0$, $\varepsilon_8 = 2\varepsilon_0$, $\varepsilon_9 = \varepsilon_0$, $d_1 = 2.5$ $\mu$m, $d_2$–$d_8 = 2$ $\mu$m, $\rho_{\text{polysilicon}} = 0.01\ \Omega$ cm, $h_1 = 0.5$ $\mu$m, and $h_2 = 2.5$ $\mu$m)

| Number of nodes | $K$ | Dominant pole (P) $\times 10^{13}$ | Residue (R) $\times 10^{12}$ | P-relative error (%) | R-relative error (%) | CPU time (s) |
|---|---|---|---|---|---|---|
| 24 | 1,1,1 | −1.675877 | 12.61800 | 41.32 | 39.80 | 3.6 |
| 64 | 2,2,1 | −1.404943 | 10.68733 | 18.48 | 18.41 | 28.8 |
| 96 | 2,2,2 | −1.353656 | 9.457056 | 14.15 | 4.780 | 64.0 |
| 120 | 3,3,1 | −1.341787 | 10.40872 | 13.15 | 15.32 | 107.1 |
| 192 | 4,4,1 | −1.316535 | 10.31855 | 11.02 | 14.33 | 294.1 |
| 216 | 3,3,3 | −1.257249 | 9.021230 | 6.022 | 0.04836 | 387.1 |
| 360 | 3,3,6 | −1.240282 | 9.224103 | 4.591 | 2.199 | 1125.6 |
| 384 | 4,4,4 | −1.211498 | 9.005094 | 2.164 | 0.2271 | 1368.3 |
| 600 | 5,5,5 | −1.185834 | 9.025595 | 0.0 | 0.0 | 4012.6 |

element; and the condition ($c$) is else. The parameters of $Z$, $D$, $r_1$, $r_2$, $l_1$, $l_2$, and $L$ are shown in Fig. 2; the parameter of $A_j$ is the area of the $j$th triangular element; the term $\tan^{-1}(y/x)$ in Equation (21) is defined to take a value in $(-\pi, \pi]$ as the counterclockwise angle from $x$-axis in $xy$-plane.

According to the layout data, an automatic mesh generation takes place, in which node numbers and their coordinates are linked to the pre-processor of boundary element tools. Hence, it has been pointed out[7] that the calculated capacitance values are sensitive with respect to selection of nodes. To examine the accuracy and the efficiency of sinusoidal weighing method, we employ the following scheme within each other of vertex points, $\boldsymbol{r}_{i,\text{vertex1}}$ and $\boldsymbol{r}_{i,\text{vertex2}}$, in which one takes

$$\boldsymbol{r}_{i,k} = \left(\frac{\boldsymbol{r}_{i,\text{vertex2}} + \boldsymbol{r}_{i,\text{vertex1}}}{2}\right) - \left(\frac{\boldsymbol{r}_{i,\text{vertex2}} - \boldsymbol{r}_{i,\text{vertex1}}}{2}\right) \times \left(\cos\frac{(k-1)\pi}{K}\right)^n, \tag{24}$$

where $k = 1, 2, \ldots, K$; $\boldsymbol{r}_{i,k}$ is the position for the $k$th node of the $i$th conductor and $n$ is the weighing factor.

## 4. RESULTS AND COMPARISON

The most obvious application of our proposed method is to determine how much changes in voltages on a given conductor to capacitively transmit to nearby conductor in inhomogeneous dielectric material oriented over an infinite ground plane. For the general case, we consider the scenario described in Fig. 1, in which a voltage step is applied to the near end of $M_1$ conductor. Actually, when the pumping charges are driven to one end of conductor, according to the image charges induced by the multiconductors on multilayer topography we adopted, the coupling capacitance of interconnections becomes complicated to analyze. The voltage responses at both the far ends of the parallel conductors are monitored, in which $M_2$ has its near end grounded. For this configuration, typically one end of every conductor is driven and the other end is connected to a high-impedance input, which can be considered as open.

For the convenience of monitoring, all the values in the tables but not all the figures listed are calculated at far end of $M_1$ conductor. The accuracy of the proposed method could be checked against data in Table 1 for two parallel conductors and inhomogeneous dielectric material ($\varepsilon_1 = 12\varepsilon_0$, $\varepsilon_2 = 10\varepsilon_0$, $\varepsilon_3 = 8\varepsilon_0$, $\varepsilon_4 = 6\varepsilon_0$, $\varepsilon_5 = 5\varepsilon_0$, $\varepsilon_6 = 4\varepsilon_0$, $\varepsilon_7 = 3\varepsilon_0$, $\varepsilon_8 = 2\varepsilon_0$, $\varepsilon_9 = \varepsilon_0$, $d_1 = 2.5$ $\mu$m, $d_2$–$d_8 = 2$ $\mu$m, $\rho_{\text{polysilicon}} = 0.01\ \Omega$ cm, $h_1 = 0.5$ $\mu$m and $h_2 = 2.5$ $\mu$m) oriented over an infinite ground plane shown in Fig. 1. One can see from Table 1 that the relative error of dominant pole will converge to less than about 6% for the number of nodes larger than 216 under equal-space meshing and the CPU time will be less than 388 s. To investigate the effectiveness of the sinusoidal weighing scheme, which has been proven with efficiency[7], we calculate the dominant poles for Fig. 1 under different grid-partition con-

Table 2. The effectiveness of the sinusoidal weighing scheme for Fig. 1. ($\varepsilon_1 = 12\varepsilon_0$, $\varepsilon_2 = 10\varepsilon_0$, $\varepsilon_3 = 8\varepsilon_0$, $\varepsilon_4 = 6\varepsilon_0$, $\varepsilon_5 = 5\varepsilon_0$, $\varepsilon_6 = 4\varepsilon_0$, $\varepsilon_7 = 3\varepsilon_0$, $\varepsilon_8 = 2\varepsilon_0$, $\varepsilon_9 = \varepsilon_0$, $d_1 = 2.5$ $\mu$m, $d_2$–$d_8 = 2$ $\mu$m, $\rho_{\text{polysilicon}} = 0.01\ \Omega$ cm, $h_1 = 0.5$ $\mu$m, and $h_2 = 2.5$ $\mu$m, and the total number of nodes = 216)

| Number of nodes | $K$ | $n$ | Dominant pole (P) $\times 10^{13}$ | Residue (R) $\times 10^{12}$ | P-relative error (%) | R-relative error (%) | CPU time (s) |
|---|---|---|---|---|---|---|---|
| 600 | 5,5,5 | – | −1.185834 | 9.025595 | 0.0 | 0.0 | 4012.6 |
| 216 | 3,3,3 | – | −1.257249 | 9.021230 | 6.022 | 0.04836 | 387.1 |
| 216 | 3,3,3 | 0.1 | −1.536966 | 17.15946 | 29.61 | 90.12 | 375.3 |
| 216 | 3,3,3 | 0.3 | −1.402907 | 13.44055 | 18.31 | 48.92 | 377.9 |
| 216 | 3,3,3 | 0.5 | −1.315606 | 10.92545 | 10.10 | 21.05 | 376.8 |
| 216 | 3,3,3 | 0.7 | −1.278199 | 10.07221 | 7.789 | 11.60 | 376.9 |
| 216 | 3,3,3 | 0.9 | −1.259367 | 9.587981 | 6.201 | 6.231 | 383.1 |
| 216 | 3,3,3 | 1 | −1.254386 | 9.424369 | 5.781 | 4.418 | 374.8 |
| 216 | 3,3,3 | 3 | −1.308487 | 9.243864 | 10.34 | 2.418 | 365.3 |
| 216 | 3,3,3 | 5 | −1.320206 | 8.540574 | 11.33 | 5.374 | 385.6 |
| 216 | 3,3,3 | 7 | −1.329681 | 7.839647 | 12.13 | 13.14 | 358.9 |
| 216 | 3,3,3 | 9 | −1.334477 | 7.536269 | 12.58 | 16.50 | 380.5 |

Table 3. The effectiveness of the Padé-via-Lanezos (PVL) algorithm for Fig. 1. ($\varepsilon_1 = 12\varepsilon_0$, $\varepsilon_2 = 10\varepsilon_0$, $\varepsilon_3 = 8\varepsilon_0$, $\varepsilon_4 = 6\varepsilon_0$, $\varepsilon_5 = 5\varepsilon_0$, $\varepsilon_6 = 4\varepsilon_0$, $\varepsilon_7 = 3\varepsilon_0$, $\varepsilon_8 = 2\varepsilon_0$, $\varepsilon_9 = \varepsilon_0$, $d_1 = 2.5\ \mu$m, $d_2$–$d_8 = 2\ \mu$m, $\rho_{\text{polysilicon}} = 0.01\ \Omega$ cm, $h_1 = 0.5\ \mu$m, and $h_2 = 2.5\ \mu$m, and the total number of nodes = 216)

| Number of nodes | $q$ | Dominant pole (P) $\times 10^{13}$ | Residue (R) $\times 10^{12}$ | P-relative error (%) | R-relative error (%) | CPU time (s) |
|---|---|---|---|---|---|---|
| 216 | 1 | −1.364759 | 10.71526 | 8.551 | 18.78 | 284.0 |
| 216 | 2 | −1.269978 | 10.47836 | 1.012 | 16.15 | 286.3 |
| 216 | 3 | −1.298798 | 10.65753 | 3.305 | 18.14 | 286.3 |
| 216 | 4 | −1.305764 | 10.72842 | 3.859 | 18.92 | 287.2 |
| 216 | 5 | −1.270067 | 9.781184 | 1.020 | 8.424 | 286.8 |
| 216 | 6 | −1.259597 | 9.221521 | 0.1868 | 2.220 | 288.9 |
| 216 | 7 | −1.260981 | 9.313396 | 0.2968 | 3.239 | 285.7 |
| 216 | 8 | −1.257346 | 9.030531 | 0.007715 | 0.1031 | 286.0 |
| 216 | 180 | −1.257249 | 9.021230 | 0.0 | 0.0 | 387.1 |

ditions, as shown in Table 2. The second and third rows are calculated under equal-space meshing as references for other sinusoidal weighing conditions. From Table 2, it can be found that the relative error will grow as n value is both larger and less than 1. Obviously, the sinusoidal weighing method for the transient cases has no particular advantage as compared to the steady case[7], due to the complex charge pumping process. It is should be noted that the computation time is made on HP-735 workstation, which depends not only on the algorithm presented here but also on the method of grid partition. Furthermore, the pole/residue representation of the Padè approximation of $H_q$ can be obtained by running the Lanczos algorithm and by computing an eigen decomposition of the Lanczos matrix $T_q$. From Table 3, as the number of computed poles $q$ is increased, one can see more and more accurate approximation of the poles. At the same time, the $H_q$ approximation form is more and more approaching the exact frequency response $H$. It is worth to note that under equal-space meshing for $q = 8$, the relative error is only about 0.007715% and the CPU time is greatly reduced to about 30% of the value under equal-space meshing in the tenth row with $q = 180$.

In order to illustrate the flexibility of our proposed technique, we consider more general cases with different values of the ground plane position and dielectric constants for multilayers. Two different cases for transient characteristics are analyzed. For the first case, we consider the influence of the ground plane in a stratified inhomogeneous dielectric medium ($h_2$ is a variable, $h_1 = 0.5\ \mu$m, $\varepsilon_1 = 12\varepsilon_0$, $\varepsilon_2 = 10\varepsilon_0$, $\varepsilon_3 = 8\varepsilon_0$, $\varepsilon_4 = 6\varepsilon_0$, $\varepsilon_5 = 5\varepsilon_0$, $\varepsilon_6 = 4\varepsilon_0$, $\varepsilon_7 = 3\varepsilon_0$, $\varepsilon_8 = 2\varepsilon_0$, $\varepsilon_9 = \varepsilon_0$, $d_1 = 2.5\ \mu$m, $d_2$–$d_8 = 2\ \mu$m, $\tau_1 = \varepsilon_1/\sigma$, and the total number of nodes = 216), shown in Fig. 1. Comparisons with these capacitances under steady state are made in Table 4, which are calculated by BFEM[7], where $C_{ii}$ is the ground capacitance and $C_{ij}$ is the coupling capacitance. In Table 4, it is a inhomogeneous dielectric medium case and we can see the consistency between the results with its transient phenomena shown in Figs 3 and 4, which monitor the far ends of $M_1$ and $M_2$ conductors, respectively. The transient current of $M_1$ conductor is capacitively transmitted to the $M_2$ conductor and the ground plane. So, the conductor nearby the ground plane has larger ground capacitance and transient current to the ground plane, resulting in slower rising time, as shown in Fig. 3. Accordingly, the larger coupling capacitance results in the larger transient current to $M_2$ conductor and at the same time the larger voltage response of cross talk occurs, as shown in Fig. 4.

In the second case, different permitivities of inhomogeneous dielectric material ($\varepsilon_2$–$\varepsilon_9$ are variables, $\varepsilon_1 = 12\varepsilon_0$, $h_1 = 0.5\ \mu$m, $h_2 = 2.5\ \mu$m, $d_1 = 2.5\ \mu$m, $d_2$–$d_8 = 2\ \mu$m, and the total number of nodes = 216) are oriented over an infinite ground plane shown in Fig. 1 and comparisons of these capacitance data[7] are made in Table 5. The results with transient phenomena shown in Figs 5 and 6 monitor the far ends of $M_1$ and $M_2$ conductors, respectively. Whereas, it's interesting to note that the larger total capacitance of $M_1$ conductor is due to the larger

Table 4. Comparisons of computed capacitances for different vertical positions of the conductor $M_1$ in homogeneous medium ($h_2$ is a variable, $h_1 = 0.5\mu$m, $\epsilon_1 = 12\epsilon_0$, $\epsilon_2 = 10\epsilon_0$, $\epsilon_3 = 8\epsilon_0$, $\epsilon_4 = 6\epsilon_0$, $\epsilon_5 = 5\epsilon_0$, $\epsilon_6 = 4\epsilon_0$, $\epsilon_7 = 3\epsilon_0$, $\epsilon_8 = 2\epsilon_0$, $\epsilon_9 = \epsilon_0$, $d_1 = 2.5\ \mu$m $d_2 - d_8 = 2\mu$m, and the total number of nodes = 216) over the ground plane shown in Fig. 1

| $h_2$ (in $\mu$m) | $C_{11}$ (in fF) | $C_{12} = C_{21}$ (in fF) | $C_{22}$ (in fF) | Dominant pole (P) $\times 10^{13}$ | Residue (R) $\times 10^{12}$ |
|---|---|---|---|---|---|
| 2.5 | 1.1349504 | 0.23096465 | 0.6664932 | −1.257249 | 9.021230 |
| 4.5 | 1.2369053 | 0.06489628 | 0.5894202 | −1.335456 | 10.42261 |
| 6.5 | 1.2677952 | 0.02904903 | 0.4645599 | −1.341432 | 10.53949 |
| 8.5 | 1.2798277 | 0.01603546 | 0.3783433 | −1.342607 | 10.55964 |
| 10.5 | 1.2856113 | 0.01013377 | 0.3045548 | −1.343004 | 10.56757 |
| 12.5 | 1.2890541 | 0.00670949 | 0.2320600 | −1.343167 | 10.56859 |
| 14.5 | 1.2913719 | 0.00438618 | 0.1607427 | −1.343251 | 10.57229 |
| 16.5 | 1.2934351 | 0.00233123 | 0.0931514 | −1.343316 | 10.58283 |
| 18.5 | 1.2942815 | 0.00150988 | 0.0767692 | −1.343328 | 10.57293 |

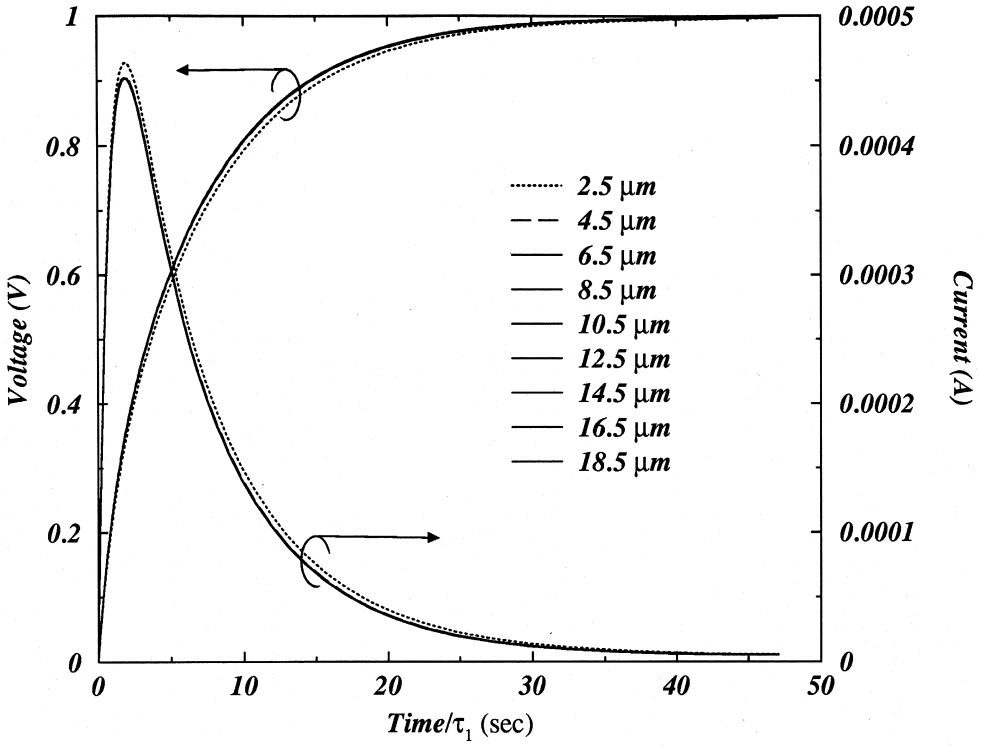


Fig. 3. The transient characteristics for the end of the conductor $M_1$ vs different vertical positions of the conductor $M_1$ in inhomogeneous medium ($\varepsilon_1 = 12\varepsilon_0$, $\varepsilon_2 = 10\varepsilon_0$, $\varepsilon_3 = 8\varepsilon_0$, $\varepsilon_4 = 6\varepsilon_0$, $\varepsilon_5 = 5\varepsilon_0$, $\varepsilon_6 = 4\varepsilon_0$, $\varepsilon_7 = 3\varepsilon_0$, $\varepsilon_8 = 2\varepsilon_0$, $\varepsilon_9 = \varepsilon_0$, $d_1 = 2.5$ $\mu$m, $d_2$–$d_8 = 2$ $\mu$m, $\rho_{\text{polysilicon}} = 0.01$ $\Omega$ cm, $h_1 = 0.5$ $\mu$m and $h_2 = 2.5$ $\mu$m, $\tau_1 = \varepsilon_1/\sigma$, and the total number of nodes = 216) over the ground plane shown in Fig. 1.

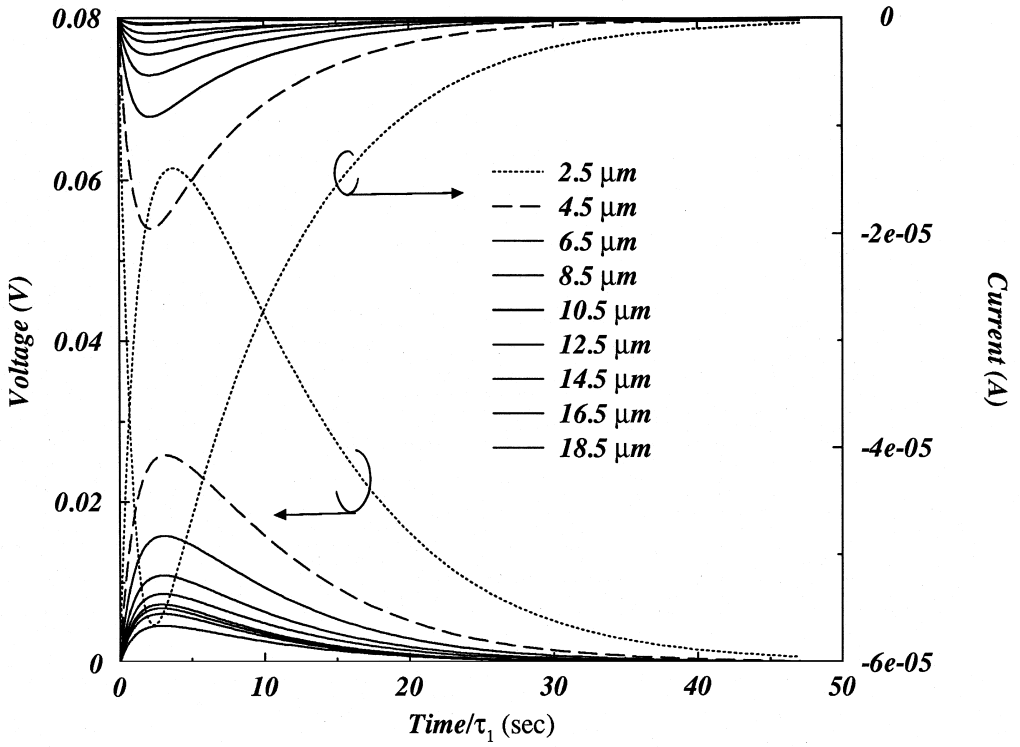


Fig. 4. The transient characteristics for the end of the conductor $M_2$ vs different vertical positions of the conductor $M_1$ in homogeneous medium ($\varepsilon_1 = 12\varepsilon_0$, $\varepsilon_2 = 10\varepsilon_0$, $\varepsilon_3 = 8\varepsilon_0$, $\varepsilon_4 = 6\varepsilon_0$, $\varepsilon_5 = 5\varepsilon_0$, $\varepsilon_6 = 4\varepsilon_0$, $\varepsilon_7 = 3\varepsilon_0$, $\varepsilon_8 = 2\varepsilon_0$, $\varepsilon_9 = \varepsilon_0$, $d_1 = 2.5$ $\mu$m, $d_2$–$d_8 = 2$ $\mu$m, $\rho_{\text{polysilicon}} = 0.01$ $\Omega$ cm, $h_1 = 0.5$ $\mu$m and $h_2 = 2.5$ $\mu$m, $\tau_1 = \varepsilon_1/\sigma$, and the total number of nodes = 216) over the ground plane shown in Fig. 1.

Table 5. Comparisons of computed capacitances for two parallel conductors in different permitivities of inhomogeneous dielectric material ($h_1 = 0.5\ \mu$m, $h_2 = 2.5\ \mu$m, $d_1 = 2.5\ \mu$m, $d_2$–$d_8 = 2\ \mu$m, the total number of nodes = 216, $\varepsilon_1 = 12\varepsilon_0$, and $\varepsilon_2$–$\varepsilon_9$ are variables (1) $\varepsilon_2$–$\varepsilon_9 = 1.0$, 0.8, 0.6, 0.5, 0.4, 0.3, 0.2, 0.1 $\varepsilon_0$; (2) $\varepsilon_2$—$\varepsilon_9 = 10$, 8, 6, 5, 4, 3, 2, 1 $\varepsilon_0$; (3) $\varepsilon_2$–$\varepsilon_9 = 100$, 80, 60, 50, 40, 30, 20, 10 $\varepsilon_0$) oriented over an infinite ground plane shown in Fig. 1

| $\varepsilon_2$ (in $\varepsilon_0$) | $C_{11}$ (in fF) | $C_{12} = C_{21}$ (in fF) | $C_{22}$ (in fF) | Dominant pole (p) $\times 10^{13}$ | Residue (R) $\times 10^{12}$ |
|---|---|---|---|---|---|
| 1.0 | 1.2143509 | 0.15929757 | 0.7180898 | −1.352663 | 10.46842 |
| 10.0 | 1.1349504 | 0.23096465 | 0.6664932 | −1.257249 | 9.021230 |
| 100.0 | 1.1430249 | 0.26650206 | 4.9028508 | −1.280641 | 10.67617 |

permittivity in the above 2th dielectric layers, resulting in the larger transient current flowing from $M_1$ conductor to $M_2$ conductor and the ground plane. So, the slower rising time of voltage for $M_1$ conductor occurs at the same time, as shown in Fig. 5. Accordingly, the larger coupling capacitance $C_{12}$ is due to the larger permittivity in the above 2th dielectric layers, resulting in the larger transient current to $M_2$ conductor. Nevertheless, the larger total capacitance of $M_2$ conductor is due to the larger permittivity in the above 2th dielectric layers, resulting in the larger transient current flowing from $M_2$ conductor to $M_1$ conductor and the ground plane. So, the larger voltage response of cross talk occurs at the same time, as shown in Fig. 6. Furthermore, it is worth to note that the phase of the transient current is leading to one of the transient voltage, as depicted in Figs 4 and 6. From the above analysis, it's important to incorporate the consideration of multilayer topography for modeling the transient characteristics of multilevel interconnection.

## 5. CONCLUSIONS

To model the transient characteristics of distributed resistor–capacitor of ULSI multilevel interconnections on complex topography, we have proposed an efficient method to avoid the redundant works on both volume mesh and transient analysis associated with the finite-difference method. Based on the conservation of charge, the boundary-element integral formulation associated with the PVL algorithm is reconstructed to analyze efficiently the transient characteristics, in which arbitrary triangular elements on the surface of conductors for charge distribution are used to calculate the free-charge distribution for arbitrary configurations of the multilevel conductor system in a inhomogeneous med-

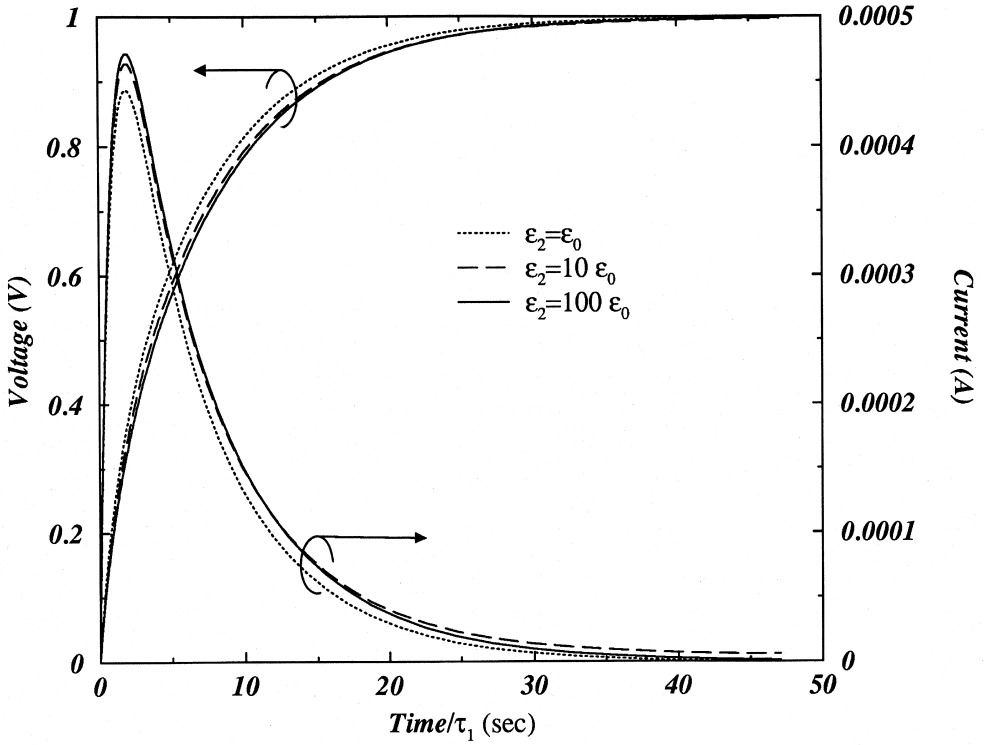


Fig. 5. The transient characteristics for the end of the conductor $M_1$ vs different permitivities of inhomogeneous dielectric material ($h_1 = 0.5\ \mu$m, $h_2 = 2.5\ \mu$m, $d_1 = 2.5\ \mu$m, $d_2$–$d_8 = 2\ \mu$m, the total number of nodes = 216, $\varepsilon_1 = 12\varepsilon_0$, $\tau_1 = \varepsilon_1/\sigma$, and $\varepsilon_2$–$\varepsilon_9$ are variables: (1) $\varepsilon_E$–$\varepsilon_9 = 1.0$, 0.8, 0.6, 0.5, 0.4, 0.3, 0.2, 0.1 $\varepsilon_0$; (2) $\varepsilon_2$–$\varepsilon_9 = 10$, 8, 6, 5, 4, 3, 2, 1 $\varepsilon_0$; (3) $\varepsilon_2$–$\varepsilon_9 = 100$, 80, 60, 50, 40, 30, 20, 10 $\varepsilon_0$) oriented over an infinite ground plane shown in Fig. 1.

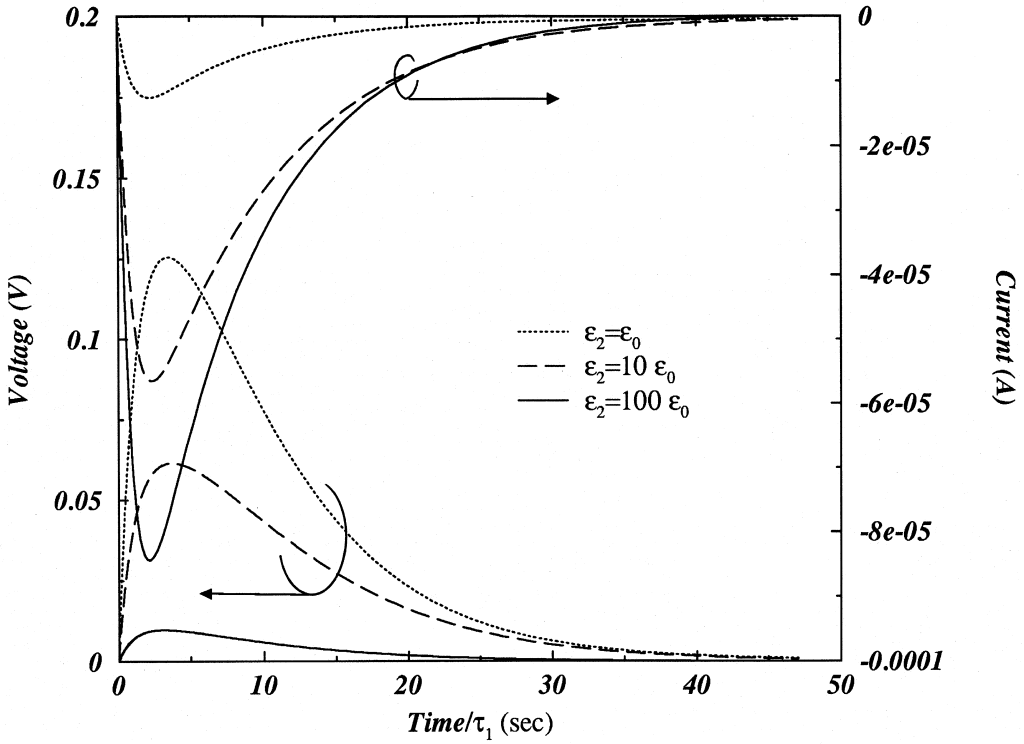


Fig. 6. The transient characteristics for the end of the conductor $M_2$ vs different permitivities of inhomogeneous dielectric material ($\varepsilon_2$–$\varepsilon_9$ are variables, $\varepsilon_1 = 12\varepsilon_0$, $h_1 = 0.5\ \mu$m, $h_2 = 2.5$ mm, $d_1 = 2.5\ \mu$m, $d_2$–$d_8 = 2\ \mu$m, $\tau_1 = \varepsilon_1/\sigma$, and the total number of nodes = 216) oriented over an infinite ground plane shown in Fig. 1

ium. The actual topography of the multilevel conductor system becomes more realistic in modeling its transient characteristics. For this purpose, our work uses an adaptive multilayer closed-form spatial Green's function for BEM to examine the voltage and current responses of the multilevel conductor system. By introducing the closed-form spatial Green's function, we can efficiently deal with the number of layer more than three, as compared with the method using the full-form Green's function in[9]. All of the surface integrals of charge distribution have been discretized after the use of Galerkin principle over boundary elements. To improve computation efficiency, we have adopted constant element for discritization, which can be evaluated analytically. To cope with the poor timing analysis efficiency of the finite-difference method, arbitrary numbers of poles and residues are generated by introducing the Padè-via-Lanczos (PVL) algorithm with little numerical degradation. The formulations of poles and residues are derived, which can be calculated fast enough to be easily included in a circuit simulator. Hence, it is easy to calculate the transient characteristics of both parallel conductors and complicated configurations such as crossing lines, corners, contacts, multilayers and their combinations. From our analysis, it has been pointed out that incorporation of the consideration of multilayer topography for modeling the transient characteristics of multilevel interconnection is important and necessary. Moreover, our reformulation algorithm can also be applied to even more complex topography, which has been proven by the merge of boundary-element method (MBEM)[8]. Major improvements are the reformulation of BEM and PVL with multilayer closed-form spatial Green's function to model the transient characteristics, which are proven to be applicable to even more complex configuration. These improvements have made possible to link with existing CAD tools.

## REFERENCES

1. Rubinstein, J., Penfield, P. and Horowitz, M. A.Jr., Signal delay in RC tree networks, *IEEE Trans. Computer-Aids Design– 2*, 1983, **CAD,** 202.
2. Yang, P. and Chatterjee, P. K., SPICE modeling for small geometry MOSFET circuits, *IEEE Trans. Computer-Aided Design– 1*, 1982, **CAD,** 169.
3. Van Der Meijs, N. P. and Van Genderen, A. J., Space-efficient extraction algorithm, in *Proc. IEEE 3rd European Design Automation Conference*, Brussels, Belgium, 1992, p. 520.
4. Pillage, L. T. and Rohrer, R. A., Asymptotic waveform evaluation for timing analysis, *IEEE Trans. Computer-Aids Design– 9*, 1990, **CAD,** 352.
5. Kumashiro, S., Rohrer, R. A. and Strojwas, A. J., Asymptotic waveform evaluation for transient analysis of 3-D interconnect structures, *IEEE Trans. Computer-Aids Design– 12*, 1993, **CAD,** 988.

6. Chou, M. and White, J., Efficient reduced-order modeling for the transient simulation of three-dimensional interconnect, in *Proceedings of the 32th Design Automation Conference*, 1995, p. 40.
7. Hou, H. M., Sheen, C. S. and Wu, C. Y., A novel modeling technique for efficiently computing 3-D capacitances of VLSI multilevel interconnections – BFEM, *IEEE Trans. Electron Devices*, 1998, ED–45,200.
8. Hou, H. M., Sheen, C. S. and Wu, C. Y., A novel 3-D capacitance modeling for ULSI multilevel interconnections on complex topography, *IEEE Trans. Computer-Aided Design*. Submitted.
9. Hou, H. M., Sheen, C. S. and Wu, C. Y., A novel transient simulation for 3-D multilevel interconnections on complex topography, *IEEE Trans. Electron Devices*. Submitted.
10. Ling, D. D., Kim, S. and White, J., A boundary-element approach to transient simulation of three-dimensional integrated circuit interconnect, in *Proceedings of the 29th Design Automation Conference*, 1992, p. 93.
11. Feldmann, P. and Freund, R. W., Efficient linear circuit analysis by Padé approximation via the Lanczos process, *IEEE Trans. Computer-Aids Design– 14*, 1995, **CAD,** 639.
12. Fukui, T., Fukuhara, T. and Furuichi, T., Three-dimensional analysis of a fresh water lens in an island, *Proceedings of U.S. Japan Seminar on BEM: Boundary Element Methods in Applied Mechanics*, 1988, p. 285.
13. Oh, K. S., Kuznetsov, D. B. and Schutt-Aine, J. E., Capacitance computations in a multilayered dielectric medium using closed-form spatial Green's functions, *IEEE Trans. Microwave Theory Techniques– 42*, 1994, **MTT,** 1443.